Shallow Water Models for Efficiently Visualizing Fluid Flow in Complex Topography Areas

Bandung Arry Sanjoyo, *Member, IAENG*, Diana Purwitasari, Mochammad Hariadi, Kikuchi Tsukasa, Mauridhi Hery Purnomo, *Member, IAENG*

Abstract— Numerous serious game applications require the visualization of fluid flow that contains information about flow depth and velocity in wet/dry complex topography areas. Fluid flow visualization based on the numerical solutions of shallow water equations (SWEs) in wet/dry areas remains a challenging problem at present, because most methods are numerically unstable. In this work, we propose a stable and efficient strategy for visualizing fluid flow in various topography areas in the wet/dry domain. In the proposed framework, the visualization covers flow depth and velocity. First, we transform the commonly used conservative SWE model into the proposed non-conservative SWE model. Second, we create an algorithm based on the discretization scheme of the proposed model. The algorithm involves few numerical operations, and is stable and accurate. Finally, we verify the results by comparing them with analytical solutions and with the solutions of the conservative model. According to the numerical results, the solution of the proposed model is close to the analytical solutions, and the proposed model can successfully visualize fluids in complex topography areas in wet or wet/dry conditions.

Index Terms— fluid flow visualization, non-conservative model, shallow water equations

I. INTRODUCTION

EXTENSIVE research has explored fluid applications [1]. Fluid applications such as water floods and tsunamis exert considerable impact on property and life. Reducing the impact, requires the development of serious games for flood disasters [2]. Serious games are an effective approach to engaging people to understand flood disasters [3]. Such game requires the visualization of fluid flow which contains information about physical quantities, such as flow depth and velocity. Flow visualization can be carried out through experiments or by using computational fluid dynamics based on Navier-Stokes equations. The visualization of fluid flow involves displaying the pattern of fluid flow to obtain the qualitative and quantitative information from fluid characteristics, such as velocity and pressure [4]. The physical information of fluids is crucial in serious game applications.

The Navier-Stokes equations were introduced to simulate fluid on computer graphics by Foster et al. [5], and Harlow-Welch [6]. Stam combined an implicit method and a Lagrangian (i.e., a semi-Lagrangian method) to visualize fluids [7]. This method is stable in long time steps and allows users to interact in real time with three-dimensional fluids. However, the two methods do not contain variables that represent fluid depth.

In order to obtain the depth of flow, the Navier-Stokes equation was derived into Shallow Water Equations (SWEs). SWEs have recently been used to model problems, such as river flow [8], [9], dam-break flow [10], [11], ocean wave [12], and tsunami [13], [14]. These existing studies focused on the wet domain area, or watery domain, but they did not consider flow from wet to dry domain areas. Alghosoun et al. simulated fluid in dry regions by reformulating the SWEs into new systems [15]. Their reformulation focused only on tracking the point of interface between the wet/dry region and then solving the problem up to that point. Moreover, they did not test the new system on various domain areas. Hence, the systems have yet to be guaranteed to work on complex topography areas.

Several approaches have been used to simulate the flow in wet/dry areas by modifying the computational strategy without reformulating the system. Takahashi simulated debris flow based on formulation approximated by Euler's continuum equation and by using experimental data [16]. Adzkiya and Sanjoyo used Takahashi's approach to predict the debris flow distribution in a downhill of Merapi volcano from a wet area to a dry area on the basis of an SWE with sediment transport [17]. This simulation only works on specific domain areas or topographies, especially downhill areas. Touma and Kanbar recently developed a second-order central scheme for the numerical solution of a two-dimensional system of SWEs featuring wet and dry states over varying water beds [18]. However, their approach has high computational complexity.

Bandung Arry Sanjoyo, Department of Electrical Engineering, Institut Teknologi Sepuluh Nopember, Surabaya, Indonesia, e-mail: bandung@matematika.its.ac.id.

Diana Purwitasari, Department of Informatics, Institut Teknologi Sepuluh Nopember, Surabaya, Indonesia, e-mail: diana@if.its.ac.id.

Mochammad Hariadi, Department of Electrical Engineering, Institut Teknologi Sepuluh Nopember, Surabaya, Indonesia, e-mail: mochar@ee.its.ac.id.

Kikuchi Tsukasa, School of Science, Tokyo University of Technology, Tokyo, Japan, e-mail: kikuchitks@stf.teu.ac.jp.

Mauridhi Hery Purnomo, Department of Electrical Engineering, Institut Teknologi Sepuluh Nopember, Surabaya, Indonesia, e-mail: hery@ee.its.ac.id.

This study focuses on developing a stable and efficient (low cost) strategy for the visualization of fluid flow in wet/dry domain area and complex bed topographies. The physical parameters of fluid flow are the depth and velocity of flow. Under the proposed strategy, the SWE model is changed into a new model that combines conservative and non-conservative models. Then, a numerical scheme with low-cost computation is selected, and transformed into an efficient algorithm. The algorithm is subsequently tested. The advantage of the new model is its capability of visualizing various types of fluid flow in wet/dry domain and complex topography areas.

The flow visualization based on the proposed model is implemented using MATLAB to verify the reliability of the model and its numerical scheme. To verify the results, we compare the numerical results and the analytical steady-state solutions for subcritical flow, trans-critical flow, and super-critical flow. The visualization of fluid flow in wet and dry domains with flat, bumps, sabo, blocks, and other complex topographies is also conducted.

II. MODELING AND VISUALIZATION STRATEGY

A. Fluid Flow Model

The essential concepts in fluid visualization are the fluid flow model, numerical simulation, and realistic visualization of fluid flow. Fluid movement is governed by a fluid flow model called the Navier-Stokes equation as in (1)-(2) [19].

$$\nabla \cdot U = 0 \tag{1}$$

$$\partial_t U = -(U \cdot \nabla)U + \nu \nabla^2 U + \left(g - \frac{\nabla p}{\rho} \right) \tag{2}$$

where $\nabla = \left(\partial_x, \partial_y, \partial_z \right)$ is a differential operator with respect to space, $\partial_t = \partial / \partial t$, $\partial_x = \partial / \partial x$, $\partial_y = \partial / \partial y$, $\partial_z = \partial / \partial z$,

$U = U(x, y, z, t) = \left(u, v, w \right)^T$ is the velocity flow vector, p is flow pressure, ρ is fluid density, ν is kinematic viscosity, and g is the force vector working on flow (e.g., gravity force). The variable u, v, and w are the velocity components with respect to x, y, and z, respectively. Equations (1)-(2) describe an incompressible free surface fluid. The solution of (1)-(2) provides information about the pressure and velocity of flow at each node position and at a certain time. The Navier-Stokes equation does not contain a variable representing flow depth. Thus, it is not suitable for visualizing shallow waters, such as rivers, lakes, and coastal flows.
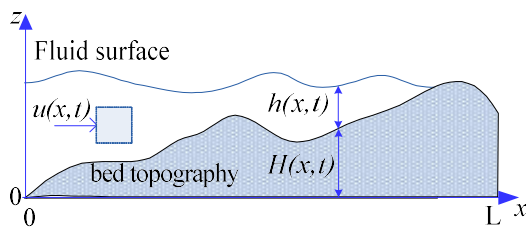

Fig. 1. Flow schema of shallow water

Rivers, lakes, or coastal flows can be viewed as shallow waters, as shown in Fig. 1. The notation $H=H(x, t)$ is the height of bed/topography in meters (m), $h=h(x, t)$ denotes the water depth in meters (m), $u=u(x, t)$ denotes the velocity

of water flow in m/s, $x \in [0, L] \subset R$ denotes the horizontal space variable in meters (m), and $t \geq 0$ is time variable in seconds (s). If (1)-(2) are applied to a shallow water and integrated over the depth of the river, then the one dimensional continuum equation (1) becomes (3). The notation $q = q(x, t) = hu$ is the flow discharge in m^2/s.

$$\partial_t h + \partial_x q = 0 \tag{3}$$

The one dimensional momentum equation (2) also becomes (4).

$$\partial_t q + \partial_x (qu + \tfrac{1}{2} g h^2) = -gh\partial_x H - ghS_f + \frac{\tau_x}{\rho} \tag{4}$$

where τ_x is stress in the x-direction, and the term S_f is the friction term. We can use Manning's law or Darcy-Weisbach's friction law for S_f.

Then, we rewrite the mathematical models of shallow water flow (3) and (4) into a conservative form, as in (5) and (6).

$$\partial_t h = -\partial_x q \tag{5}$$

$$\partial_t q = -\partial_x (qu + \tfrac{1}{2} g h^2) - gh\partial_x H - ghS_f + \frac{\tau_x}{\rho} \tag{6}$$

In a steady state flow condition, $\partial_t h = \partial_t u = 0$. Therefore, (5) becomes $\partial_t q = 0$ or $q = q_0$, where $q_0 = q(0, t)$ is the flow discharge in the initial condition. With the same approach, the momentum equation in (6) becomes (7).

$$\partial_x H = \left(\frac{q^2}{gh} - 1 \right) \partial_x h - gS_f \tag{7}$$

If we assume the absence of friction in the bed topography and integrate (7), then the flow model in steady state can be obtained as follows:

$$h^3(x) + \left(H(x) - \frac{q_0^2}{2gh_0^2} - h_0 \right) h^2(x) + \frac{q_0^2}{2g} = 0. \tag{8}$$

Equation (8) is the analytical solution of fluid flow in steady state. The equation is used to verify the flow visualization. If the initial discharge is zero, or $q_0 = 0$, then we obtain a horizontal fluid surface as in (9).

$$H(x) + h(x) = \text{constant} \tag{9}$$

Otherwise, if the initial discharge of flow is not zero, then the depth of fluid flow $h(x)$ is a polynomial cubic solution in (8) which depends on the values of q_0 and h_0.

Let us express (3) and (4) in vector notation as follows:

$$\partial_t U + \partial_x F(U) = S \tag{10}$$

where $U = \begin{pmatrix} h \\ q \end{pmatrix}$ is the conserved vector variable,

$$F(U) = \begin{pmatrix} q \\ qu + \tfrac{1}{2}gh^2 \end{pmatrix}, \text{ and}$$

$$S = \begin{pmatrix} q \\ -gh\partial_x H - ghS_f + \frac{\tau_x}{\rho} \end{pmatrix} \text{ is the vector of the source}$$

terms that depend on the elevation of the bed topography.

Equation (10) is analogous to the one-dimensional linear convection equation. It is well-known that the Lax-Friedrich numerical scheme is conditionally stable in such a system. This scheme has an accuracy of order $O(\Delta x^2, \Delta t)$, and also has low

computational complexity in terms of the number of works done [20].

The solution of the systems in (10) is (h, q). The velocity flow u can be obtained from the quantity q, that is, $u = q/h$. The range value of flow depth is $h \geq 0$. In the case of dry area, $h=0$ or $h \rightarrow 0$, we obtain $u = q / 0$ or $u = \lim_{h \to 0} q / h$, respectively. Hence, the value of flow velocity u becomes undefined or blows up to infinity. In such the case, the flow velocity is unacceptable and numerically unstable [15], [21].

To avoid zero or near-zero divisors, we propose to change (4) into another equation. Specifically, we substitute $q = hu$ into (3) and expand the derivative using the product rule to obtain (11).

$$\partial_t h + u\partial_x h = -h\partial_x u \qquad (11)$$

We use the same approach for (4) to obtain (12).

$$h\partial_t u = -2hu\partial_x u - gh\partial_x h - u(\partial_t h + u\partial_x h)$$
$$-gh\partial_x H - ghS_f + \frac{\tau_x}{\rho} \qquad (12)$$

If we ignore the stress τ_x and substitute (11) into (12), the we obtain (13).

$$\partial_t u = -\partial_x(\frac{1}{2}u^2 + gh) - g\partial_x H - ghS_f \qquad (13)$$

We still use (3) because we want to preserve the flow discharge in the unit variable q. Hence, we propose another form of SWE systems, which is a combination of conservative and non-conservative forms. In compact form, we express the new system of SWE in (14).

$$\partial_t U = -\partial_x F(U) + S \qquad (14)$$

Where $U = \begin{pmatrix} h \\ u \end{pmatrix}$ is the conserved vector variable, $F(U) = \begin{pmatrix} hu \\ \frac{1}{2}u^2 + gh \end{pmatrix}$, and $S = \begin{pmatrix} 0 \\ -g\partial_x H - ghS_f \end{pmatrix}$. For simplicity, we call the proposed SWE system in (14) the non-conservative SWE system.

From (14), we can obtain the solution (h, u) numerically. The computation process of obtaining flow depth h and flow velocity u does not involve the variable divisor h. Numerically, the SWE systems in (14) is more stable than the SWE system in (10). The Jacobian matrix of (15) is $J_F = \partial F / \partial U$ with eigenvalues $\lambda_1 = u + \sqrt{gh}$ and $\lambda_2 = u - \sqrt{gh}$. As in linear advection equation, λ_1 and λ_2 are the speeds of advection.

B. Computational Strategy

In computing flow visualization, the computational cost is the main factor, but the accuracy of the results is still considered. Several finite difference schemes, such as Lax-Friedrichs, Lax-Wendroff, and leapfrog, are available to solve partial differential equations. Although, the three numerical schemes have the same order of time complexity, $O(N)$, in each time step, the number of works done by Lax-Friedrichs scheme is only half of those of the Lax-Wendroff and leapfrog schemes. Therefore, we choose the Lax-Friedrichs discretization scheme because it is more efficient in terms of the number of works done in each time step. Furthermore, it has a low computational cost and the order of accuracy is quadratic in space and linear in time, i.e., $O(\Delta x^2, \Delta t)$.

In Lax-Friedrichs scheme, time and space discretization is achieved using the forward time, centered space scheme [22]. To stabilize this scheme, Lax-Friedrichs defines U_i^k as the average of U_{i-1}^k and U_{i+1}^k or $U_i^k = \frac{1}{2}(U_{i-1}^k + U_{i+1}^k)$. Thus, the time derivative in (14) becomes (15).

$$\partial_t U = \frac{U_i^{k+1} - \frac{1}{2}(U_{i-1}^k + U_{i+1}^k)}{\Delta t} \qquad (15)$$

The space discretization uses the central difference scheme as in (16), to obtain an accuracy of order $O(\Delta x^2)$.

$$\partial_x F(U) = \frac{F_{i+1}^k - F_{i-1}^k}{2\Delta x} \qquad (16)$$

The calculation of flow parameter $U = (h\ u)^T$ is based on (14). As the left-hand side of (14) is the derivative of U with respect to time t, the strategy of obtaining the values of U_i^{k+1} at time $t = k+1$ is based on (17).

$$U_i^{k+1} = (U_{i+1}^k - U_{i-1}^k) / 2 - \Delta t(-\partial_x F(U) + S) \qquad (17)$$

Here, the initial values of variable $U_0 = (h_0, u_0)^T$ are set. The stability of the scheme is achieved when the CFL σ is less than or equal to 1, that is, $\sigma = c\frac{\Delta t}{\Delta x} \leq 1$, where $c = \max\{\lambda_1, \lambda_2\}$. Hence, we obtain inequality in (18)

$$\Delta t_i \leq \frac{\Delta x}{\max_{i=1..N}\{|u_i + \sqrt{gh_i}|, |u_i - \sqrt{gh_i}|\}} \qquad (18)$$

In order to measure the error of numerical solution, we use the L_1 norm error as in (19).

$$L_1 = \sum_{i=1}^N \frac{|u_i^c - u_i^e|}{N} \qquad (19)$$

where u_i^c denotes the numerical solution, u_i^e denotes the analytical solution both on node i.

C. Flow Visualization Algorithm

Based on the discretization results, the algorithm for visualizing fluid flow can be stated as follows.

Input : Time of visualization t and initial discretization time Δt_0, the height of topography H_i, and the initial values of the fluid flow parameters h_i^0, and u_i^0,

Output : Fluid flow parameters h_i^{k+1}, h_i^{k+1}, and the visualization of fluid flow.

Algorithm:

1. Initialization step:
   - Variable geometric grids, H_i, and dH/dx.
   - Variable flow height h_i^0, and flow velocity u_i^0.

2. For each time step do:
   - Calculate Δt_i using (18), which must satisfy CFL condition.
   - Calculate vector U_i^{k+1} using (17).
   - Apply the boundary conditions.
   - Visualize the flow variables h_i^{k+1} and h_i^{k+1}.
   End of time loop

In each time step, the number of works done by the algorithm is linear in space, i.e. $O(N)$ where N is the number of nodes in the grid depending on Δx. Furthermore, the time interval Δt_i is adaptive with respect to space discretization, flow velocity, and the flow depth parameters as shown in (18).

III. ANALYSIS OF VISUALIZATION RESULTS

As stated in the Introduction, a serious game is used as an educational platform to recognize and understand the characteristics and distribution of flood. Therefore, we choose a number of complex topographies that are close to those in the real world. These topographies include flat, flat with bumps, downhill with blocks, parabolic, downhill with sabo, and coastal area topographies. To verify the correctness of the proposed model, we visualize the following various types of flow:

1. Fluid flow in a wet area consists of lake at rest under steady state, transcritical flow under steady state, and supercritical flow under steady state. In this case, we compare the numerical results of the proposed model (non-conservative SWE model) and the analytical solutions in (8) and (9). We also compare the proposed model and the conservative SWE model.
2. Fluid flow in wet/dry area consists of dam-break flow over the dry domain, wet/dry domain in parabolic areas, and flow in semi-natural wet/dry area.

### A. Lake at rest under steady state

Lake at rest under steady state is a subcritical fluid flow in domain area that is totally immersed. The domain topographies are flat, flat with bumps or blocks, and downhill with blocks. As the results of some cases are similar, we only show the fluid flow visualizations for flat topography and flow in a downhill with blocks. Fig. 2 presents the fluid flow visualization for flat topography. We have domain $x \in [0, L]$, $L = 15\,m$, flat topography ($H(x) = 0$ m), and no discharge at the boundary or $q_0 = q_{15} = 0\,m^2/s$. Initially, we set the dam-break at location $x = 5\,m$. The flow depth in domain $0\,m \leq x \leq 5\,m$ is $h(x) = 5\,m$ and that in the right side of the dam $5\,m \leq x \leq 15\,m$, $h(x) = 2\,m$. The dam break at time $t = 0\,s$. The solid line graphs depict the flow depth and velocity according to the conservative SWE model. The graphs with light dashed lines depict the flow depth and velocity based on the non-conservative SWE model. As shown in Fig. 2 (a) and Fig. 2 (b), the graphs of flow depth and velocity are almost the same at $t = 0\,s$, $t = 0.47\,s$, $t = 1.43\,s$, and $t = 472.37\,s$ in the conservative and non-conservative SWE models. The flow depths and velocities at $t = 472.37\,s$ (see Fig. 2 (b)) and beyond are constant, and the flow velocity $u(x) = 0\,m/s$. This result means that the water flow is at rest and is consistent with (9).

Fig. 3 presents the fluid flow visualization for a downhill with block topography. The domain is $[0, 25]$. The topography is downhill and has a block at the right end. The boundary has no discharge, $q_0 = q_{25} = 0\,m^2/s$. Initially, we set the dam break at location $x=10\,m$. The flow depth on the

left side of the dam is $h=5m$, and that on the right side of the dam is $h=2m$. Fig. 3 (a) depicts this initial condition. The dam break is set at time $t=0s$. The solid line graphs depict the flow depth and velocity based on the conservative SWE model. The graphs with light dashed lines depict the flow depth and velocity based on the non-conservative SWE model. The graphs of flow depth and velocity are almost the same at $t=2.89\ s$, and $t=1621.70\ s$ in the conservative and non-conservative SWE models, as shown in Fig. 3 (b). After a long period, the flow depth is almost constant and the flow velocity $u(x) \to 0m/s$. Hence, the water flow is at rest and is consistent with (9).
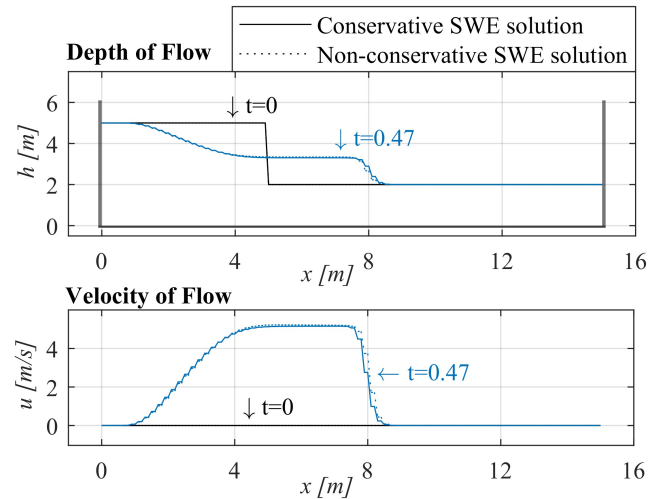
(a)
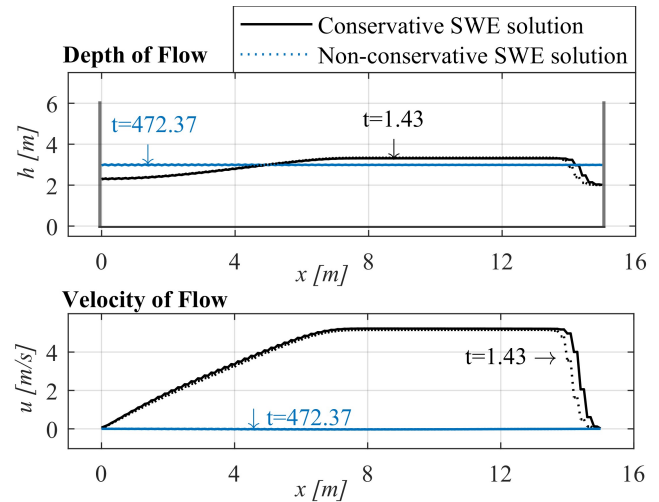
(b)

Fig. 2. Fluid flow from dam break to steady-state for flat topography

B. Transcritical flow under steady state

In the case of transcritical flow under steady state, we use the flow condition set by Lundgren [14]. When fluid flows over a flat area with a bump (see Fig. 4) and given $h_L = 0.66$ m, and $q_0 = 1.53\ m^2/s$, the flow achieves a steady state with flow depth as in (20).

$$h^3(x) + \left(H(x) - \frac{q_0^2}{2gh_c^2} - h_c - H_M\right)h^2(x) + \frac{q_0^2}{2g} = 0 \quad (20)$$

where $H_M = \max\limits_{x\in[0,L]} H(x)$, h_c is the fluid depth above H_M, and $H(x)$ is described in (21).

$$H(x) = \begin{cases} 0.2 - 0.05(x-10)^2 & \text{if } 8m < x < 12m, \\ 0 & \text{otherwise} \end{cases} \quad (21)$$
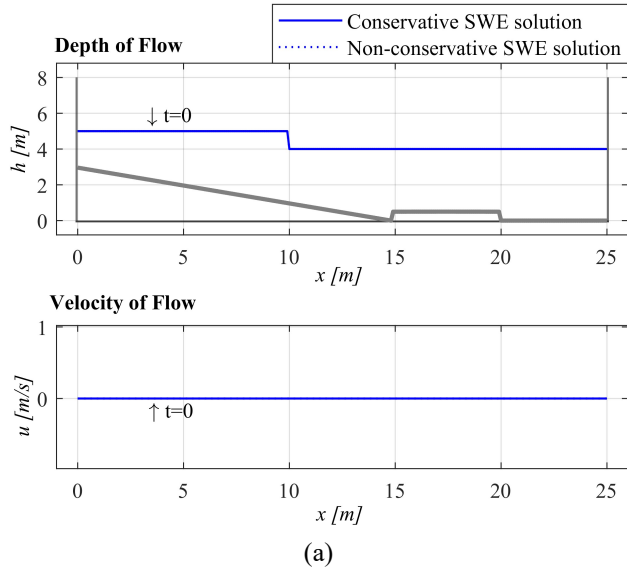

(a)

(b)

Fig. 3. Fluid flow from dam break to steady-state for a downhill with block topography

Fig. 4 depicts the visualization of steady-state transcritical flow over a flat area with bumps. The initial flow depth is 0.66 m, and the discharge is 1.53 m^2/s. The solid line graph depicts the flow depth and velocity from the steady-state analytical solution. The graphs with dotted lines depict the flow depth and velocity based on the non-conservative SWE model. The graphs with dashed-dotted lines depict the flow depth and velocity based on the conservative SWE model. From Fig. 4 (a), the flow depths and velocities obtained from the conservative and non-conservative models show the same pattern and close to each other for $t \le 1.02 s$. However, for $t > 10 s$, the non-conservative model is closer to the steady-state analytical solution than the conservative

model as shown in Fig. 4 (b). When time $t > 30 s$, they move toward the steady-state analytical solution with L_1 error less than 0.1 m or less than 15% as shown in Fig. 5.
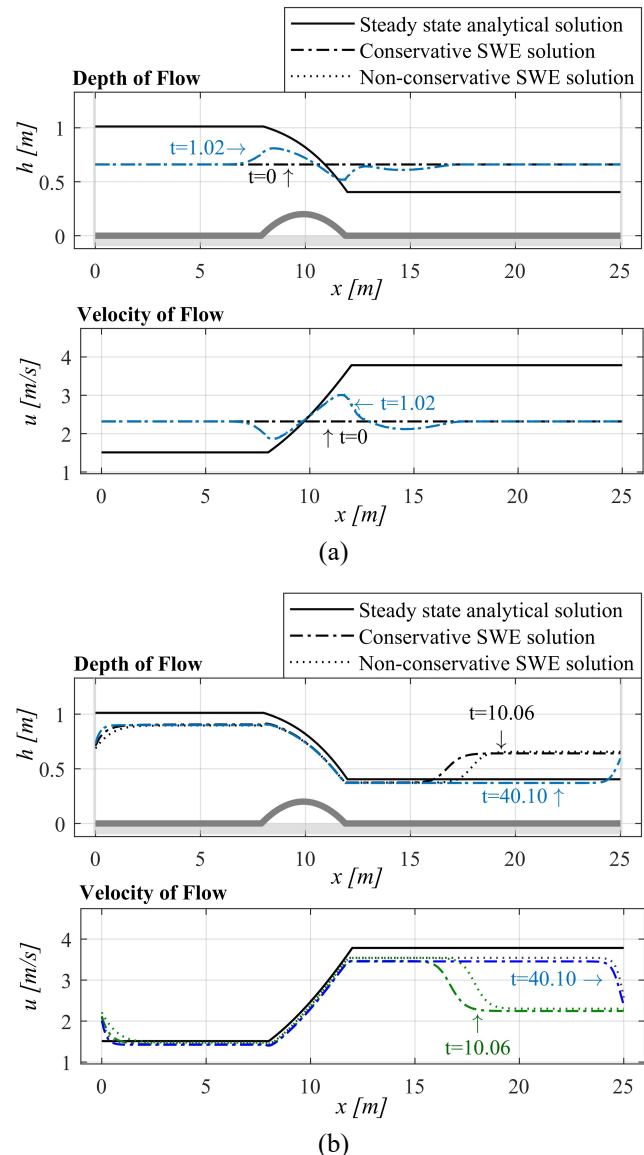

(a)

(b)

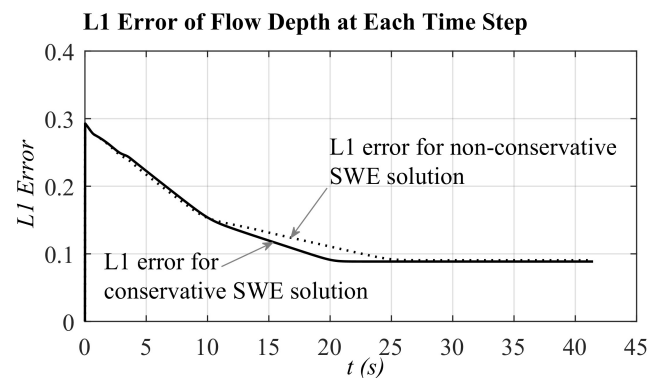Fig. 4. Transcritical flow in steady state over a flat area with bumps

Fig. 5. L_1 Error of flow depth based on conservative and non-conservative SWE for steady-state transcritical flow

C. Supercritical flow under steady state

In the case of supercritical flow, steady-state occurs over a flat area with bumps (see Fig. 6). The flow depth $h_L = 0.33$ m, and the discharge $q_0 = 0.103$ m^2/s. In this case, the flow over 0 $m \leq x \leq 8$ m is subcritical, the flow above the bumps is supercritical, and the flow over 12 $m \leq x \leq 25$ m becomes subcritical [23]. The flow near the upper right of the bumps is a hydraulic jump. Thus, the analytical solution in domain 0 $m \leq x \leq 8$ m is (20), and the analytical solution on domain 12 $m \leq x \leq 25$ m is (8), where h_L substitutes h_0.
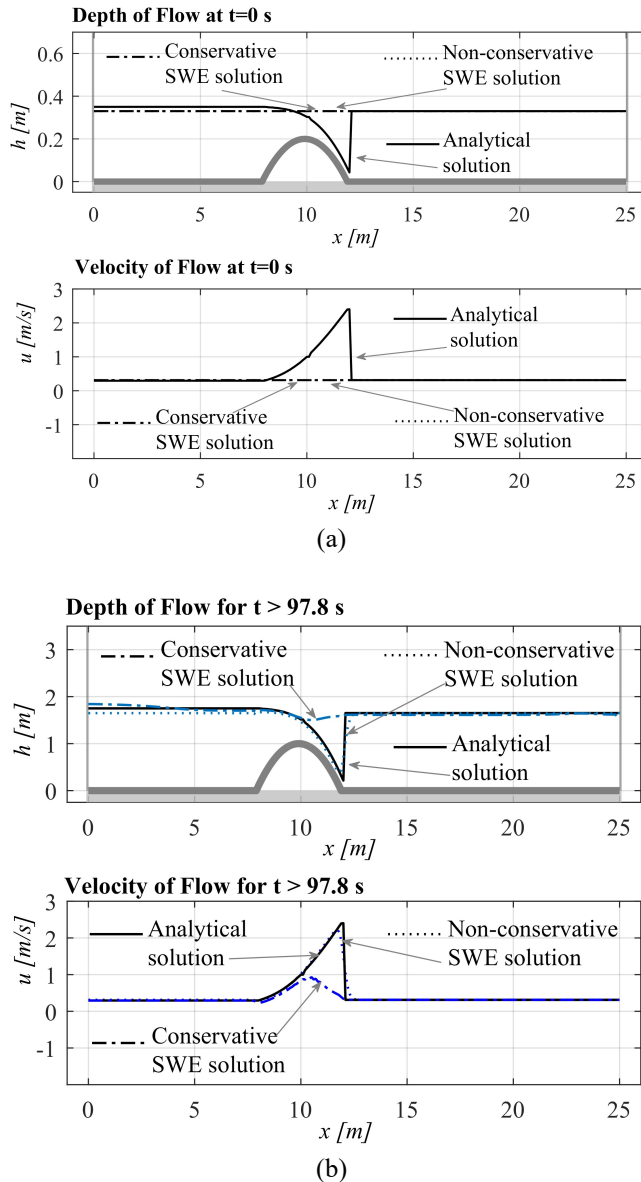

(a)

(b)

Fig. 6. Steady-state supercritical flow over a flat area with bumps

In Fig. 6, the solid line graph depicts the flow depth and velocity from the steady-state analytical solution. The graphs with dotted lines depict the flow depth and velocity based on the non-conservative SWE model. The graphs with dashed-dotted lines depict the flow depth and velocity based on the conservative SWE model. Fig. 6 (a) depicts the initial condition for conservative and non-conservative SWE model and also the analytical solution. The solution (h, u) based on the non-conservative model is considerably close to the analytical solution after time $t = 97.8$ s as shown in Fig. 6

(b). By contrast, the solution (h,u) based on the conservative SWE model is far from the analytical solution. Next, we compare the L_1 error of flow depth for conservative and non-conservative SWE model in supercritical flow as shown in Fig. 7. When the flow tend to steady-state condition, $t > 40$ s, it can be seen that the solution of non-conservative SWE model is considerably close to the analytical solution, with L_1 error less than 0.02 m or less than 6%. By contrast, the L_1 error of conservative SWE model is approximately 0.1 m or 30%. From the above comparison, we conclude that only the non-conservative SWE model can visualize supercritical flow.
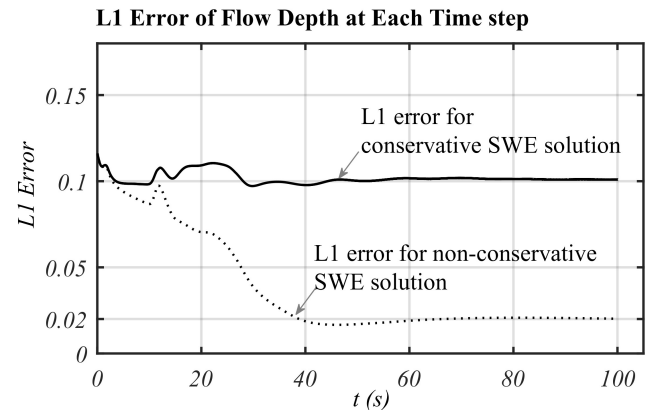

Fig. 7. L_1 error of flow depth based on conservative and non-conservative SWE model for steady-state condition in supercritical flow over a flat area with bumps

D. Dam-break flow over dry domain

Let us test the non-conservative model for fluid flow in the wet to dry domains. In the case of fluid flow in the dry domain, the conservative SWE model cannot work directly using the Lax-Friedrich scheme. We use flat topography $(H(x)=0)$ and the dam-break flow over the topography at location x_0 m. The initial condition of the flow depth is in (22).

$$h(x) = \begin{cases} h_L \geq 0m, & \text{if } 0m \leq x \leq x_0 \ m \\ 0m, & \text{if } x_0 \ m \leq x \leq 25m \end{cases} \qquad (22)$$

and $u(x) = 0$ m/s. In this case, the result of the non-conservative SWE model is compared with Ritter's analytical solution for an ideal dam-break [24]. Initially, $h_L = 5$ m and $x_0 = 10$ m.

Fig. 8 visualizes the solution of this dam-break flow. The solid line graphs depict the flow depth and velocity from the analytical solution. The graphs with dotted lines depict the flow depth and velocity based on the non-conservative SWE model. The initial condition and the solution at $t = 0.74$ s are depicted in Fig. 8 (a). Fig. 8 (b) shows the solution at $t = 1.92$ s and $t = 20.04$ s. During the time of visualization, the solution (h, u) from the non-conservative SWE model is always close to the analytical solution with L_1 error shown in Fig. 9. When $t \geq 10$ s, the L_1 error is less than 1%. When the flow tends to steady-state condition, the L_1 error is less than 0.3%.

E. Flow in wet and dry parabolic area

This section presents the capability of the non-conservative SWE model to visualize shallow water flow oscillations in a parabolic basin. In this case, the fluid moves to right and left through the wet/dry part of the parabolic basin area. The non-conservative SWE solution is compared with Thacker's analytical solution [25] and Sampson's analytical solution [26] of parabolic flow. Thacker's analytical solution is a sinusoidal periodic function that oscillates during visualization. Sampson's analytical solution is a sinusoidal periodic function with friction damping.

We compare Thacker's analytical solution with numerical result of the non-conservative SWE model. We use topography area, initial condition, and other physical parameters set by Delestre [24]. The parabolic topography is defined in (23).
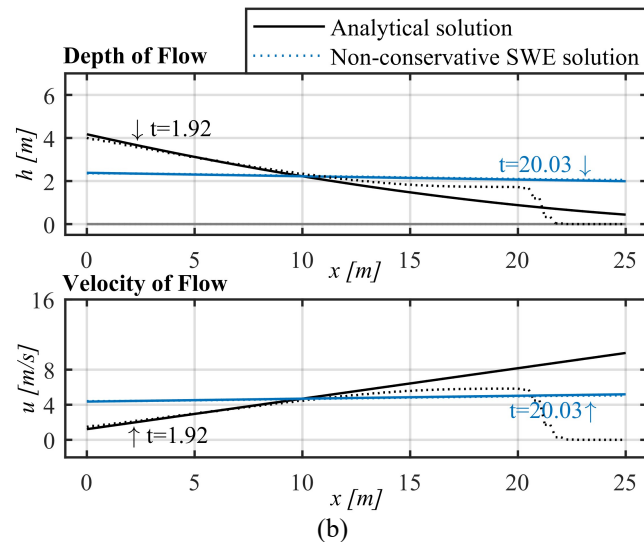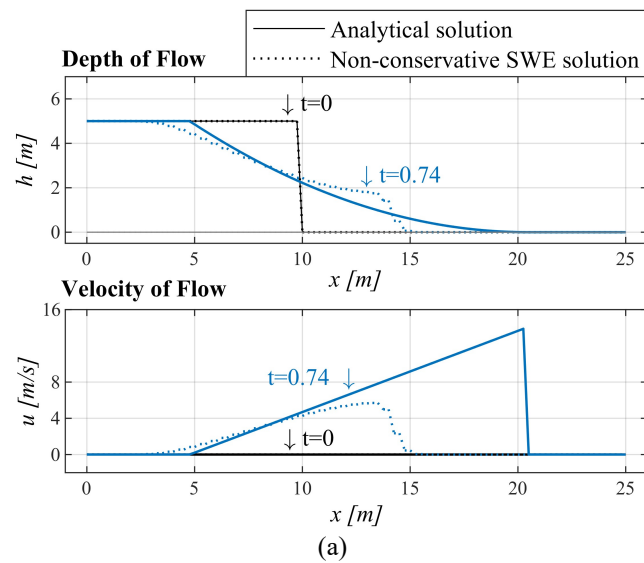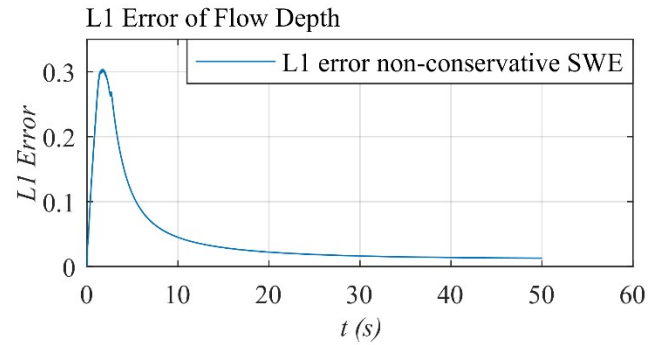
where $h_0 = 0.5\ m$, $a = 1\ m$, and $L=4\ m$.

Fig. 9. L_1 error of flow depth based on non-conservative SWE model for dam break flow over wet/dry flat area

.

(a)

(b)

Fig. 8. Dam break flow over wet/dry flat area

$$H(x) = h_0(\frac{1}{a^2}(x - \frac{L}{2})^2 - 1) \qquad (23)$$

The initial fluid velocity is $u(x) = 0\ m/s$, and the initial fluid depth is given in (24).

$$h(x) = \begin{cases} -h_0((\frac{x}{a} + \frac{1-L}{2a})^2 - 1), & \text{if } x_1 \le x \le x_2 \\ 0\,m, & \text{otherwise} \end{cases} \qquad (24)$$
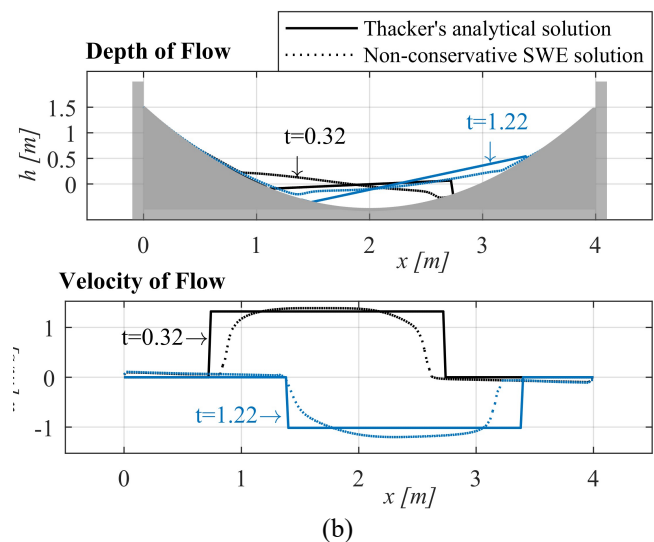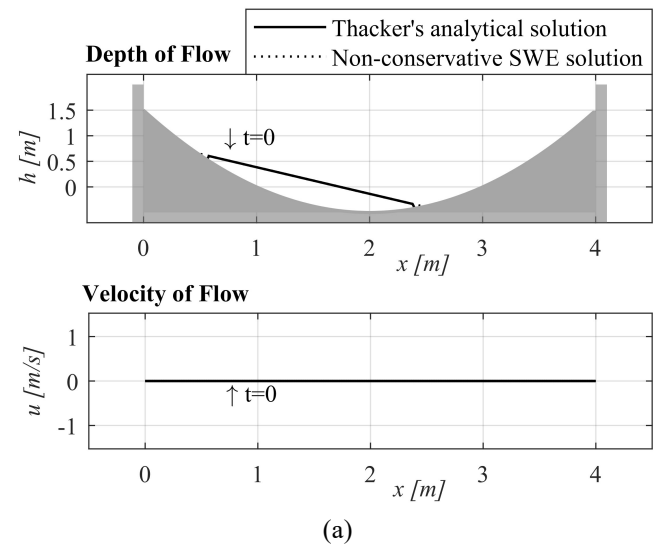

(a)

(b)

Fig. 10. Comparison between non-conservative SWE solution and Thacker's solution for shallow water oscillations

Fig. 10 (a) presents the parabolic topography and initial condition of flow depth and flow velocity. Fig. 10 (b) depicts graphical results of flow depth and velocity at $t = 0.32\ s$, and $t = 1.22\ s$. The solid lines are the graphs of flow depth and velocity from Thacker's analytical solution. The

dotted lines are the graphs of flow depth and velocity from the non-conservative SWE model. Both graphs move to the right and left almost simultaneously for three periods. However, after a long visualization, the non-conservative SWE solution moves toward a steady-state condition, and Thacker's analytical solution continues to move periodically without damping.

The second test case for shallow water oscillations uses long parabolic topography as in (23) with $h_0 = 10$ m, $a = 3,000$ m, and $L=10,000$ m. The initial flow velocity is $u(x) = 0$ m/s, and the initial flow depth uses the setting in [23]. Fig. 11 (a) presents the parabolic topography, the initial condition, and the solution at $t=557.76$ s of flow depth and flow velocity. The graphical results of flow depth and velocity at $t=941.19$ s, and $t=150,362.54$ s are shown in Fig. 11 (b). The solid lines are the graphs of flow depth and velocity from Sampson's analytical solution. The dotted lines are the graphs of flow depth and velocity from the non-conservative SWE model. Both graphs move to the right and left simultaneously. After $t >150,362.54$ s, they converge to the steady-state condition.
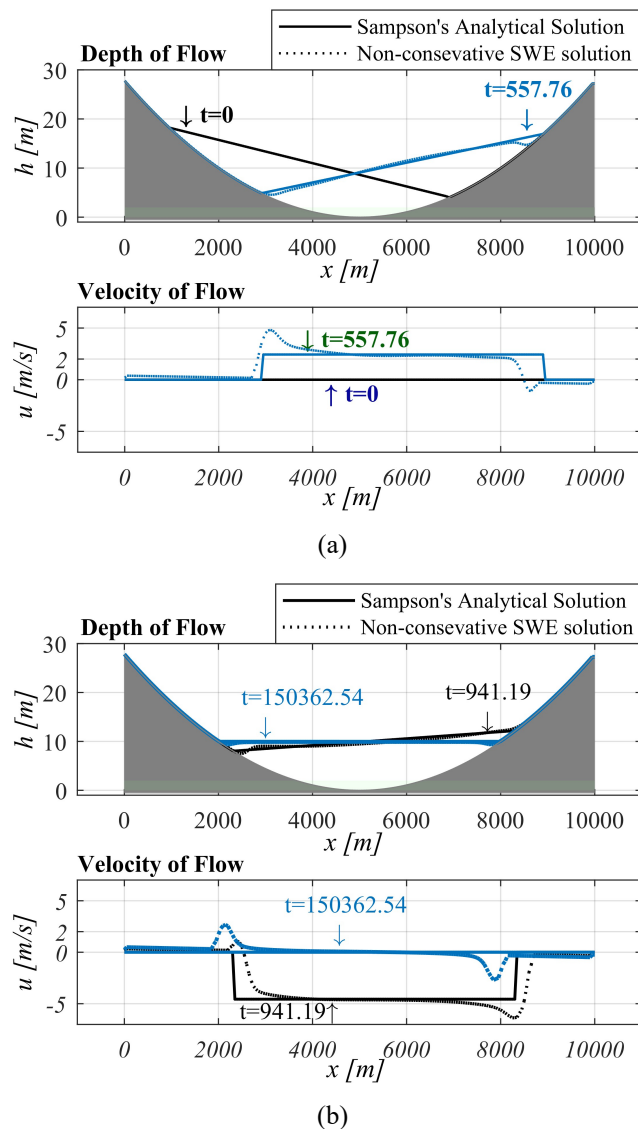

(a)

(b)

Fig. 11. Comparison between non-conservative SWE solution and Sampson's solution for shallow water oscillations

F. Flow in semi natural wet/dry area

The first case is fluid flow in a long and dry downhill area as in Fig. 12. Domain $x = [0, 200]$ m and the topography has two elevations. The first slope area has two sabo dams or bumps, similar to a downhill area in a mountain. The fluid flows from the top left side to the bottom right side. Initially, we have a dam break at the top left, $x = 0$ m, fluid depth $h_0 = 4$ m, discharge $q_0 = 14$ m^2/s. The discharge q_0 decreases exponentially with respect to time t. The colored solid lines show the fluid depth and fluid velocities. They flow down over the dry area. After $t = 8.85$ s, the fluid passes through two sabo dams before finally leaving the domain area after $t = 21.70$ s.

In the second case, the fluid flow in a semi natural wet/dry area is characterized as the coastal hydrodynamics of ocean waves on a beach. Fig. 13 shows that domain $x = [0, 200]$ m. Initially, the water level is a dam break with $u(x)=0$ m/s as shown in Fig. 13 (a). Every 3 s, a sea wave is generated at the right boundary with negative velocity. When time t increases, the seawater starts moving to the left with flow velocities $u(x) \leq 0$ m/s. Fig. 13 (b) shows the sea level $h(x)+H(x)$ and flow velocities $u(x)$ at time $t = 1.76$ s. When seawater reaches the top of the shoreline, some of its flows to the left, and the rest returns to the sea (to the right). Furthermore, sea water continues to oscillate in the shoreline area forever.
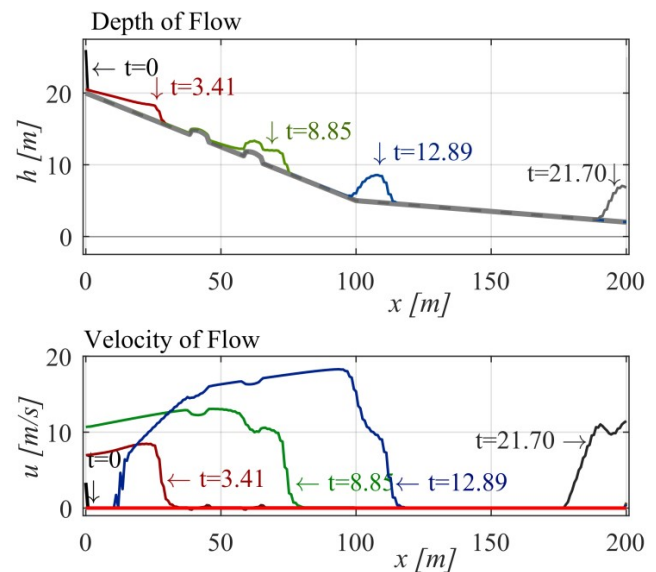

Fig. 12. Fluid flow in a downhill topography with sabo

G. Summary of visualization results

The capabilities of the conservative SWE model and the proposed SWE model (non-conservative model) to visualize fluid flow are summarized in Table I. The term "very good" means that the model can visualize the flow, and that the result is close to the analytical solution. The term "good" means that the model can visualize the flow and that it is stable. The term "poor" means that the model can visualize the flow but that the result is still far from the analytical solution. The notation "-" means that the model can not visualize the flow.

The conservative model can visualize subcritical flow and transcritical flow in wet areas only. However, the

conservative model cannot visualize supercritical flow, oscillation flow, flow in a dry downhill area, and coastal hydrodynamics. In summary, the proposed model can visualize fluid flow in many situations, such as rivers, dams, and volcanic areas under wet and wet-dry conditions. These situations are required in serious game applications. Therefore, the proposed model is suitable for serious game applications.

Table I. Summary of visualization capabilities

	Conservative model	Proposed Model
Subcritical flow in a wet area	Very good	Very good
Transcritical flow in a wet area	Very good	Very good
Supercritical flow in a wet area	Poor	Very good
Oscillation flow in a wet/dry area	-	Very good
Flow in a dry downhill area	-	Good
Coastal hydrodynamics	-	Good

IV. CONCLUSIONS

The proposed non-conservative SWE model is simpler, more stable, and more efficient (has lower complexity) than the widely available conservative SWE model. According to the test cases, the proposed model is able to visualize subcritical flow in certain complex topographies of wet areas. Moreover, the proposed model can visualize transcritical and supercritical flows. It is also able to visualize flow in wet/dry areas, such as dam break flow in a dry and flat topography, oscillation flow in a parabolic topography, flows in a dry and long downhill area, and coastal hydrodynamics of ocean waves on a beach. Hence, the proposed model could potentially be used to visualize fluid flow or flood distribution for serious game applications.

In the future, we will extend the proposed model to three-dimensional cases. In this way, it can be used to visualize fluid flows for serious game applications in real environments. Furthermore, we are also interested in modeling time-varying bed topographies. In this case, the model can be used to visualize sedimentation and bed erosion.

REFERENCES

[1] Itishree Nayak, "Numerical Study of MHD Flow and Heat Transfer of an Unsteady Third Grade Fluid with Viscous Dissipation," IAENG International Journal of Applied Mathematics, vol. 49, no. 2, pp245-252, 2019

[2] M.-H. Tsai, Y.-L. Chang, J.-S. Shiau, and S.-M. Wang, "Exploring the effects of a serious game-based learning package for disaster prevention education: The case of Battle of Flooding Protection," International Journal of Disaster Risk Reduction, vol. 43, 101393, 2020.

[3] M. Khoury et al., "A Serious Game Designed to Explore and Understand the Complexities of Flood Mitigation Options in Urban–Rural Catchments," Water, vol. 10, no. 12, 1885, 2018.
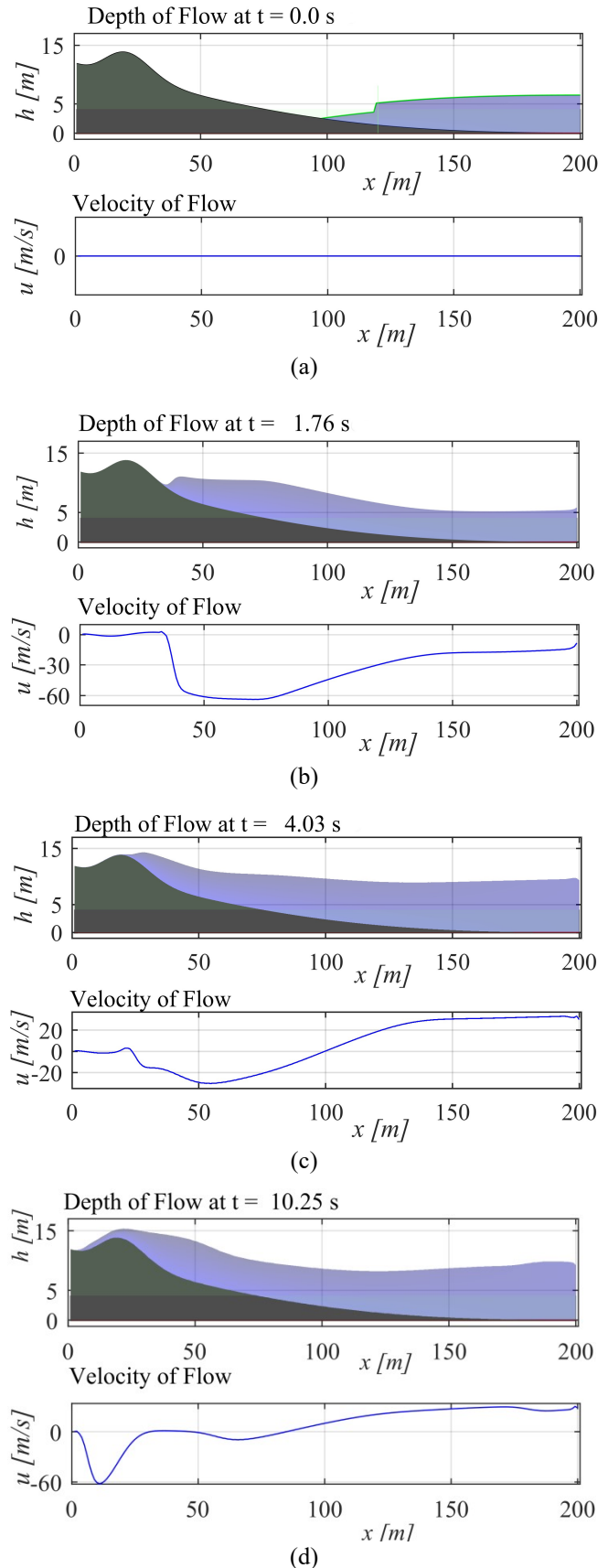
Fig. 13. Coastal hydrodynamics of ocean waves on a beach

[4] M. Raissi, A. Yazdani, and G. E. Karniadakis, "Hidden fluid mechanics: A navier-stokes informed deep learning framework for assimilating flow visualization data," arXiv preprint arXiv:1808.04327, 2018.

[5] N. Foster and D. Metaxas, "Modeling the Motion of a Hot, Turbulent Gas," In Proceedings of the 24th annual conference on Computer

graphics and interactive techniques (SIGGRAPH '97), ACM Press/Addison-Wesley Publishing Co., USA, 1997, pp. 181-188.

[6] F. Harlow and J. E. Welch, "Numerical Calculation of Time-Dependent Viscous Incompressible Flow of Fluid with Free Surface," The Physics Fluids, vol. 8, no. 12, pp. 2182–2189, 1965.

[7] J. Stam, "Stable Fluids," in SIGGRAPH '99 Conference Proceedings, Los Angeles, USA, 1999, pp. 121–128.

[8] N. Gouta and F. Maurel, "A finite volume solver for 1D shallow-water equations applied to an actual river," International Journal Numerical Methods in Fluids, vol. 38, no. 1, pp. 1–19, 2002.

[9] A. Decoene, L. Bonaventura, E. Miglio, and F. Saleri, "Asymptotic derivation of the section-averaged shallow water equations for natural river hydraulics," Mathematical Models and Methods in Applied Sciences, vol. 19, no. 03, pp. 387–417, 2009.

[10] Wu Weiming and Wang Sam S., "One-Dimensional Modeling of Dam-Break Flow over Movable Beds," Journal of Hydraulic Engineering, vol. 133, no. 1, pp. 48–58, 2007.

[11] Y. Ni, Z. Cao, and Q. Liu, "Mathematical modeling of shallow-water flows on steep slopes," Journal of Hydrology and Hydromechanics, vol. 67, no. 3, pp. 252–259, 2019.

[12] University of Hormozgan and F. Rashidi, "An Efficient Finite Element Method for Numerical Modeling of Shallow Water Wave Propagation," International Journal of Intelligent Engineering and Systems, vol. 9, no. 3, pp. 156–162, 2016.

[13] M. Zuhair and S. Alam, "Tsunami Impacts on Nuclear Power Plants along Western Coast of India Due to a Great Makran Earthquake: A Numerical Simulation Approach," International Journal of Geosciences, vol. 8, no. 12, pp. 1417–1426, 2017.

[14] L. Lundgren, "Efficient numerical methods for the shallow water equations," Uppsala Universitet, Uppsala, 2018.

[15] A. Alghosoun, M. Herty, and M. Seaid, "Numerical Modeling of Wave Run-Up in Shallow Water Flows Using Moving Wet/Dry Interfaces," International Journal of Mechanical and Mechatronics Engineering, vol. 11, no. 10, pp. 1757-1761, 2018.

[16] T. Takahashi, Debris Flow: Mechanics, Prediction and Counter measures, London: CRC Press, 2nd edition, 2014.

[17] B. A. Sanjoyo and D. Adzkiya, "One and two dimensional debris flow simulation using finite difference method," presented at the International Conference on Mathematical Applications in Engineering (ICMAE'10), Kuala Lumpur, Aug. 2010.

[18] R. Touma and F. Kanbar, "Well-balanced central schemes for two-dimensional systems of shallow water equations with wet and dry states," Applied Mathematical Modelling, vol. 62, pp. 728–750, 2018.

[19] M. Griebel, T. Dornseifer, and T. Neunhoeffer, Numerical Simulation in Fluid Dynamics: A Practical Introduction, Philadelphia: SIAM, 1998.

[20] B. A. Sanjoyo, M. Hariadi, and M. H. Purnomo, "Stable Algorithm Based On Lax-Friedrichs Scheme for Visualization of Shallow Water," EMITTER International Journal of Engineering Technology, vol. 8, no. 1, pp. 19–34, 2020.

[21] S. Bi, J. Zhou, Y. Liu, and L. Song, "A Finite Volume Method for Modeling Shallow Flows with Wet-Dry Fronts on Adaptive Cartesian Grids," Mathematical Problems in Engineering, vol. 2014, 2014.

[22] Geyang Guo, and Yishu Zhai, "Unconditionally Stable High Accuracy Alternating Difference Parallel Method for the Fourth-order Heat Equation," Engineering Letters, vol. 28, no.1, pp56-62, 2020

[23] H. P. Gunawan, "Numerical simulation of shallow water equations and related models," Institut Teknologi Bandung, L'Université Paris-Est, 2015.

[24] O. Delestre et al., "SWASHES: a compilation of Shallow Water Analytic Solutions for Hydraulic and Environmental Studies." Wiley, Jan. 2016.

[25] W. C. Thacker, "Some exact solutions to the nonlinear shallow-water wave equations," Journal of Fluid Mechanics, vol. 107, no. 1, pp. 499-508, 1981.

[26] J. Sampson, A. Easton, and M. Singh, "Moving boundary shallow water flow above parabolic bottom topography," Anziam Journal, vol. 47, pp. 373-387, 2005.